A semi-empirical correction for the Rayleigh-Debye-Gans approximation for fractal aggregates based on phasor analysis: Application to soot particles

Clément Argentin, Matthew Berg, Marek Mazur, Romain Ceolato, Alexandre Poux, Jérôme Yon

Version of Record: https://www.sciencedirect.com/science/article/pii/S0022407322000802
Manuscript_8b09f7694dfc36ea2ff504c801a99b94

A semi-empirical correction for the Rayleigh-Debye-Gans approximation for fractal aggregates based on phasor analysis: Application to soot particles

Clément Argentin[a], Matthew J. Berg[b], Marek Mazur[a], Romain Ceolato[c], Alexandre Poux[a], Jérôme Yon[a,*]

[a]*Normandie Univ, UNIROUEN, INSA Rouen, CNRS, CORIA, 76000 Rouen, France.*
[b]*Kansas State University, Department of Physics, 1228 N. 17th St., Manhattan, KS 66506-2601, USA*
[c]*ONERA, The French Aerospace Lab, Université de Toulouse, FR 31055, France*

Abstract

The Rayleigh Debye-Gans approximation for Fractal Aggregates (RDG-FA) is commonly used for the evaluation of the radiative properties of fractal aggregates of nanometer-scale nearly spherical particles as soot particles. The cost of its simplicity, however, is the precision of the aggregate cross sections when the refractive index deviates from unity and when the aggregate's spheres, or monomers, are not sufficiently small compared to the wavelength. While correction factors have been highlighted before, their physical origin is not clear and no universal correction factors are proposed. The present study develops an approach based on phasor analysis of the aggregate's internal electric field rigorously determined by the discrete dipole approximation. Aggregates representative of the Diffusion Limited Cluster Aggregation (DLCA) regime having a fractal dimension of $D_\mathrm{f} = 1.78$ are considered as representative of a soot aggregate. The results reveal that correction factors to the RDG-FA for forward scattering (A) and the absorption cross section (h) are due to a competition between internal-field hot-spots caused by point contact between the spherical monomers and a decrease of the field amplitude as the field propagates through the aggregate. Both phenomena are neglected in the RDF-FA by definition. The absorption phenomenon explains the aggregate-size dependence of A and h. These effects are then studied as the aggregate size varies according to the number of monomers N_m ranging from 10 to 1000, as the monomer radius varies from $R_\mathrm{m} = 5\,\mathrm{nm}$ - $30\,\mathrm{nm}$, and as the wavelength varies from $\lambda = 266\,\mathrm{nm}$ -

*Corresponding author.*E-mail address:* yon@coria.fr

1064 nm. Both constant and wavelength dependent refractive indices for organic, graphitic, and amorphous soot are considered. Finally, a semi-empirical model is proposed intended to correct the RDG-FA theory based on the analysis.
Keywords: Soot fractal aggregates, RDG-FA, Internal coupling, DDA, Phasor analysis, Scattering cross sections, Absorption cross sections

---

Highlights

- The internal electric field of fractal aggregates is studied with a phasor approach.
- Internal coupling and absorption explain the RDG-FA discrepancies for large aggregates.
- Aggregate size, monomer radius, refractive index, and wavelength dependencies are investigated.
- Semi-empirical corrections for the RDG-FA derived forward-scattering and absorption are proposed.

1. Introduction

Soot, or black carbon (BC), particles are produced by the incomplete combustion of fossil fuels and biomass. Once emitted in the atmosphere, these aerosols pose a concern for human health [1, 2], contribute actively to atmospheric radiative forcing of the climate [3], and affect atmospheric chemistry [4]. For these reasons, climate models need a simple, robust, and precise description of soot aerosol optical cross sections. Such descriptions could also serve to enhance the precision of optical diagnostics for *in-situ* characterization of similar aerosols [5] and the control of their generation for industrial purposes [6].

The absorption and scattering cross sections of aggregates can be accurately calculated by the Generalized Multiparticle Mie (GMM) [7] method and the superposition T-matrix (STM) [8] method. For soot, however, these methods are limited to aggregates of spherical particles, i.e., monomers, that are in point contact. More realistic models of soot, with overlapping monomers, necking between monomers [9], and coating of the monomers [10], are studied with the Discrete Dipole approximation (DDA) [11–13], which is not limited by particle geometry. The DDA considers a particle as a set of interacting dipoles on a cubic lattice with spacing d and yields accurate results provided that $|m|\,kd < 0.5$, where m the complex-valued refractive index and $k = 2\pi/\lambda$. Because the DDA involves a numerical cost, namely the computation time, it is not implemented in current climate models nor is it frequently used to interpret data from light scattering measurements.

For these reasons, light interaction models with simple analytical expressions are preferred, but one should be aware of their intrinsic limitations [14]. The most used one is the Rayleigh-Debye-Gans approximation [15]. The essence of this approximation is that the particle is divided into a number of small volume elements. Each element is treated as a Rayleigh scatterer (small compared to the wavelength) and the interactions between these elements are neglected. The RDG approximation can be applied to different type of aggregates like snowflake aggregates at millimeter wavelength radar [16] or aerosol Fractal Aggregates (RDG-FA) [17] as long as the criteria $|m-1| \ll 1$ and $x_m|m-1| \ll 1$ are respected. The performance of the RDG-FA is often studied in terms of the correction factors A and h, which are needed to bring the RDG-FA forward scattering and absorption, respectively, in agreement with exact calculations via the DDA. This has been studied for soot

particles [18–20] because their optical indices m do not enable the respect of the aforementioned criteria for visible light. The present authors have shown in a previous work [21] that for a bi-sphere and for typical soot materials the corrections depend on the orientation of the bi-sphere and the values of m and λ. This was explained by regions of enhanced internal electric field, i.e., hot spots, occurring at the vicinity of point contact between the monomers. Hot spots can increase or decrease the RDG-FA correction factor for forward scattering [21]. This finding is related to [20] where "positive deviations" are induced by the increase of $\mathrm{Re}\{m\}$ and "negative deviations" with increasing $\mathrm{Im}\{m\}$. The bi-sphere study [21] also reveals that the coupling distance for the monomers is relatively short. Specifically, when the monomers (spheres) center-to-center distance is larger than $4R_{\mathrm{m}}$, they can be treated as independent-scattering. This complicates the understanding of the N_{m} dependence of the A and h correction factors reported in [19, 20] which remain poorly understood [22]. Moreover, a law providing the correction factors for the RDG-FA, i.e., A and h, for all practical values of N_{m}, λ, and m, does not yet exist.

Introduced in [23, 24] and used in the aformentioned bi-sphere study [21], the method of phasor analysis can link the field within a particle to the external light scattering behavior, such as, the angular scattering pattern and cross sections. The method is unique in that it provides this link via both quantitative and graphical means, and thus, can engender understanding for the light scattering behavior of a given particle, e.g., see [24–26].

In the present study, the method is used to examine the dependence of these RDG-FA correction factors on N_{m}, λ, and m while fractal dimension and prefactor are considered constant and representative of soot particles (obtained by Diffusion Limited Cluster Aggregation [27], ≈ 1.78 and 1.4 respectively). Indeed, more compact aggregates characterized by larger fractal dimensions or prefactors will certainly have stronger interactions between monomers than more open structures, which will lead to stronger corrections. Readers interested in understanding the role played by the prefactor and the fractal dimension can find information in the work of Liu *et. al.* [28, 29]. Soot particles are very complex and their composition is generally unknown. Indeed, in the same flame, we can find nascent soot, which are mostly made of organic compounds with an amorphous carbon matrix and what is called mature soot, which are made of carbon and hydrogen atoms essentially with a certain level

of graphitization [30]. For this reason, extreme optical index behaviour will be considered (respectively graphitic, amorphous and organic soot particles) as previously studied in [31]. It may be noted that some of these indices (organic particles at lowest wavelengths) cover larger imaginary parts than those proposed by Chang and Charalampopoulos. [32]. This can be explained by the specific composition. Also, it must be noticed that Bescond *et. al.* [31] considered the fractal aggregates morphology in their inversion process whereas Chang and Charalampopoulos treated the particles as spheres. In this study, one will see the important role played by absorption within the monomers, which decreases the internal electric-field amplitude as light propagates within the aggregate material. An observation of universal trends in the phasor analysis then ultimately leads to the proposition of a semi-empirical law A and h.

2. Methodology

2.1. Fractal aggregates

This study will focus on soot aggregates that form under the diffusion limited cluster aggregation (DLCA) regime. In DLCA, a fractal scaling-law describes the average aggregate-size as [33]:

$$N_{\mathrm{m}} = k_{\mathrm{f}} \left(\frac{R_{\mathrm{g}}}{R_{\mathrm{m}}} \right)^{D_{\mathrm{f}}} \tag{1}$$

where k_{f} is a scaling prefactor, D_{f} is the fractal dimension, and R_{g} is the radius of gyration of the aggregate [17]. A selection of simulated DLCA aggregates obeying Eq.(1) is considered here. Three aggregates are taken from [20] with $N_{\mathrm{m}} = 284$, $N_{\mathrm{m}} = 444$, and $N_{\mathrm{m}} = 833$ where $D_{\mathrm{f}} = 1.78 \pm 0.04$ and $k_{\mathrm{f}} = 1.35 \pm 0.10$. To access a larger range of aggregate size, specifically $N_{\mathrm{m}} \in [10, 1000]$, a selection of 1000 different aggregates are taken from [34] where $D_{\mathrm{f}} \approx 1.78$ and $k_{\mathrm{f}} \approx 1.4$.

2.2. Internal electric field

The scattering properties of an aggregate include the total scattering C^{sca}, absorption C^{abs}, and extinction cross sections C^{ext}, in addition to the angular scattered light intensity I^{sca}. These properties can all be derived from the scattered electric field $\mathbf{E}^{\mathrm{sca}}(\mathbf{r})$, which for $\mathbf{r}$ in the aggregate's far-field zone are linked to the internal field $\mathbf{E}^{\mathrm{int}}$ inside the aggregate

material via the volume integral equation (VIE). When expressed in discrete form, i.e., for N cubic volume elements ΔV in the aggregate, the VIE reads [35]:

$$\mathbf{E}^{\mathrm{sca}}(\mathbf{r}) = \frac{k^2}{4\pi}\frac{\exp(ikr)}{r}\left(m^2-1\right)\left(\overleftrightarrow{\mathbf{I}} - \hat{\mathbf{r}}\otimes\hat{\mathbf{r}}\right)\cdot\sum_{i=0}^{N}\mathbf{E}^{\mathrm{int}}(\mathbf{r}_i)\exp(-ik\hat{\mathbf{r}}\cdot\mathbf{r}_i)\,\Delta V, \tag{2}$$

In Eq (2), $\overleftrightarrow{\mathbf{I}}$ is the Cartesian identity dyadic, $\hat{\mathbf{r}}\otimes\hat{\mathbf{r}}$ is the dyadic formed by the direct product of $\hat{\mathbf{r}}$ with itself [35, 36]. Due to the assumed far-field limit for the observation point $\mathbf{r}$, it is useful to examine the behavior of the scattered field in terms of the scattering amplitude $\mathbf{E}_1^{\mathrm{sca}}$ given from Eq. (2)

$$\mathbf{E}^{\mathrm{sca}}(\mathbf{r}) = \frac{\exp(ikr)}{r}\mathbf{E}_1^{\mathrm{sca}}(\hat{\mathbf{r}}). \tag{3}$$

Note that $\mathbf{E}_1^{\mathrm{sca}}$ depends only on direction (θ,ϕ), i.e., $\hat{\mathbf{r}}$, and not on the distance r.

The DDA method can be used to find $\mathbf{E}^{\mathrm{int}}$ accurately within the aggregate. Indeed, the DDA can be thought of as a numerical solution of Eq (2) [13]. Here, the code DDSCAT developed by [37] is used to numerically determine $\mathbf{E}^{\mathrm{int}}$. An aggregate's physical 3D shape is discretized on a cubic lattice of volume elements ΔV that are $d\times d\times d$ in size. Each element is then assigned an electric dipole moment, which are excited by the incident field and couple to each other. Following the numerical solution for value of these dipoles, i.e., the solution of Eq (2), $\mathbf{E}^{\mathrm{int}}$ can be obtained from each dipole [13]. The accuracy of the solution is determined by the fineness of this lattice as quantified by the condition $|m|\,kd < 0.5$. To satisfy this condition, a number of dipoles per monomer $N_{\mathrm{d}}/N_{\mathrm{m}}$ is specified, where N_{d} is the total number of dipoles representing an aggregate and N_{m} is the number of monomers. Below, $N_{\mathrm{d}}/N_{\mathrm{m}} \approx 110$, which is sufficient for point-contact monomers in [24] where $N_{\mathrm{d}}/N_{\mathrm{m}} \approx 34$.

The incident wave is planar, propagating along the x-axis, with linear polarization where $\mathbf{E}^{\mathrm{inc}}$ is along the y-axis in the aggregate's reference frame. Thus, $\mathbf{E}^{\mathrm{inc}}(\mathbf{r}) = E_{\mathrm{o}}\exp(ik\hat{\mathbf{x}}\cdot\mathbf{r})\hat{\mathbf{y}}$ where E_{o} is the field magnitude. A wide range of wavelengths are considered, $\lambda \in [266\,\mathrm{nm} - 1064\,\mathrm{nm}]$, and values for the refractive index appropriate for soot particles are considered. Specifically, $m = 1.75 + 1.03i$ is used from [38] as representative of mature soot (or Black Carbon) as shown by [39] for $\lambda = 550\,\mathrm{nm}$. In order to also consider the wavelength dependence of m for material other than purely graphitic or mature soot, the spectral dependence of m found in [31] for organic, graphitic, and amorphous soot compositions are also taken into account [20].

2.3. Phasor analysis

The dyadic terms in Eq. (2) will simplify if the observation point resides along the propagation of the incident wave, i.e., the forward-scattering direction, see Appxendix C in [21]. In terms of polarization, if the vertical direction is the y-axis, the incident wave is vertically polarized, which will be denoted by the subscript v. Moreover, if the scattered light is detected through a linear polarizer oriented in the vertical direction – a common configuration – then a detector measures the vertical-vertical (incident-scattered) polarization configuration, denoted by the subscript vv. The following will consider only this polarization case. Equation (2) now simplifies by virtue of Eq. (3) to give the scattering amplitude as:

$$\mathbf{E}^{\mathrm{sca}}_{1,\mathrm{vv}}(\hat{\mathbf{x}}) = \frac{3k^2}{4\pi}\frac{m^2-1}{m^2+2}E_{\mathrm{o}}\sum_{i=1}^{N_{\mathrm{d}}} z_{y,i}(\hat{\mathbf{x}})\,\Delta V\,\hat{\mathbf{y}}, \tag{4}$$

where $z_{y,i}$ is the phasor, or complex-valued number, for the i^{th} volume element. As a reminder, $\hat{\mathbf{x}}$ is the forward-scattering direction and $\hat{\mathbf{y}}$ is the vertical polarization direction. There is no distance, r, dependence in the scattering amplitude. The phasor for a volume element, or equivalently, a dipole, is determined by the internal field at the location of the element, $\mathbf{r}_i$, and by a phase factor accounting for the position of the element as

$$z_{y,i}(\hat{\mathbf{x}}) = \frac{m^2+2}{3E_{\mathrm{o}}}E^{\mathrm{int}}_y(\mathbf{r}_i)\exp\left(-ikx_i\right). \tag{5}$$

In Eq. (5), x_i is the x-component of the volume element positioned at $\mathbf{r}_i$.

Phasor analysis offers a graphical means to illustrate the contribution of each volume element to the forward scattering amplitude. It is a descriptor of the spatial variability of the internal electric field accounting for the phase shifts due to the different positions of the elements. As demonstrated in [21], the phasors are directly related to the RDG-FA correction factors for the forward differential scattering cross section:

$$A_{\mathrm{vv}}(\psi) = \frac{\frac{\mathrm{d}C^{\mathrm{sca}}_{\mathrm{vv}}}{\mathrm{d}\Omega}(0^\circ)}{\frac{\mathrm{d}C^{\mathrm{sca}}_{\mathrm{RDG,vv}}}{\mathrm{d}\Omega}(0^\circ)} = \left|\overline{z_y}\right|^2. \tag{6}$$

In Eq. (6), ψ denotes the aggregate's orientation with respect to the incident wave, $\frac{\mathrm{d}C^{\mathrm{sca}}_{\mathrm{vv}}}{\mathrm{d}\Omega}(0^\circ)$ is the true (from DDA) forward differential scattering cross section and $\frac{\mathrm{d}C^{\mathrm{sca}}_{\mathrm{RDG,vv}}}{\mathrm{d}\Omega}(0^\circ)$ is the

forward differential scattering cross section predicted by the RDG-FA. The horizontal bar denotes averaging of all the phasors in the aggregate, i.e., $\overline{z_y} = (1/V)\sum_{i=1}^{N_\mathrm{d}} z_{y,i}\,\Delta V$ where V represents the total volume of all the monomers. Further explanation for the derivation of Eq. (6) is given in Appendix F of [21]. Note that the forward scattering correction factor A refers to the average of Eq. (6) over many aggregate orientations, i.e., $A = \langle A_{\mathrm{vv}}(\psi)\rangle_\psi$, where the brackets denote orientation averaging. Here, at least 500 isotropically distributed orientations of a single aggregate or 1000 different aggregates having the same morphological descriptors, R_m, D_f, and k_f, are considered according to the reciprocity theorem [40].

3. Results

3.1. Phasor plots for a fractal aggregate

The first row of Fig. 1, plots (a) and (b), show the phasor distributions in the complex plane (horizontal axis: $\mathrm{Re}\,\{z_{y,i}\}$, vertical axis: $\mathrm{Im}\,\{z_{y,i}\}$) for an aggregate with $N_\mathrm{m} = 284$ monomers with monomer radius $R_\mathrm{m} = 15\,\mathrm{nm}$ for $\lambda = 1064\,\mathrm{nm}$ in (a) and for $\lambda = 266\,\mathrm{nm}$ in (b). That is, each point in the plot represents the complex number $z_{y,i}$ corresponding to the i^{th} volume element in the aggregate according to Eq. (5). Organic monomer-material is chosen because it is known to manifest important corrections to the RDG-FA theory [20]. This means that we take $m = 1.83 + 0.26i$ for $\lambda = 1064\,\mathrm{nm}$ and $m = 0.94 + 0.96i$ for $\lambda = 266\,\mathrm{nm}$. In both cases, $|m|$ is significant, which highlights a strong non-uniformity of the internal electric field. To see this, the plots show a unit semicircle representing the location phasors would have if their magnitude were unity $|z_{y,i}| = 1$; this corresponds to the RDG-FA prediction in case of forward scattering (see Eq 6). The average phasor, $\overline{z_y}$, is shown as the red star and is clearly outside the semicircle for $\lambda = 1064\,\mathrm{nm}$ in (a) and inside for $\lambda = 266\,\mathrm{nm}$ in (b). This indicates, respectively, an underestimation of the RDG-FA, $A > 1$, and an overestimation, $A < 1$, in accord with the findings in [19, 20]. The magnitude of the phasor distribution's spread is greater for $\lambda = 1064\,\mathrm{nm}$ with a line-like shape similar to the behaviour observed for intersecting bi-spheres in [21]. For $\lambda = 266\,\mathrm{nm}$, a more pronounced spread is seen in the distribution.

Referring again to Fig. 1(a)- 1(b), one can see that the phasor dots are colored. The meaning of these colors is to express the x_i coordinate in Eq. (5) as indicated by the color

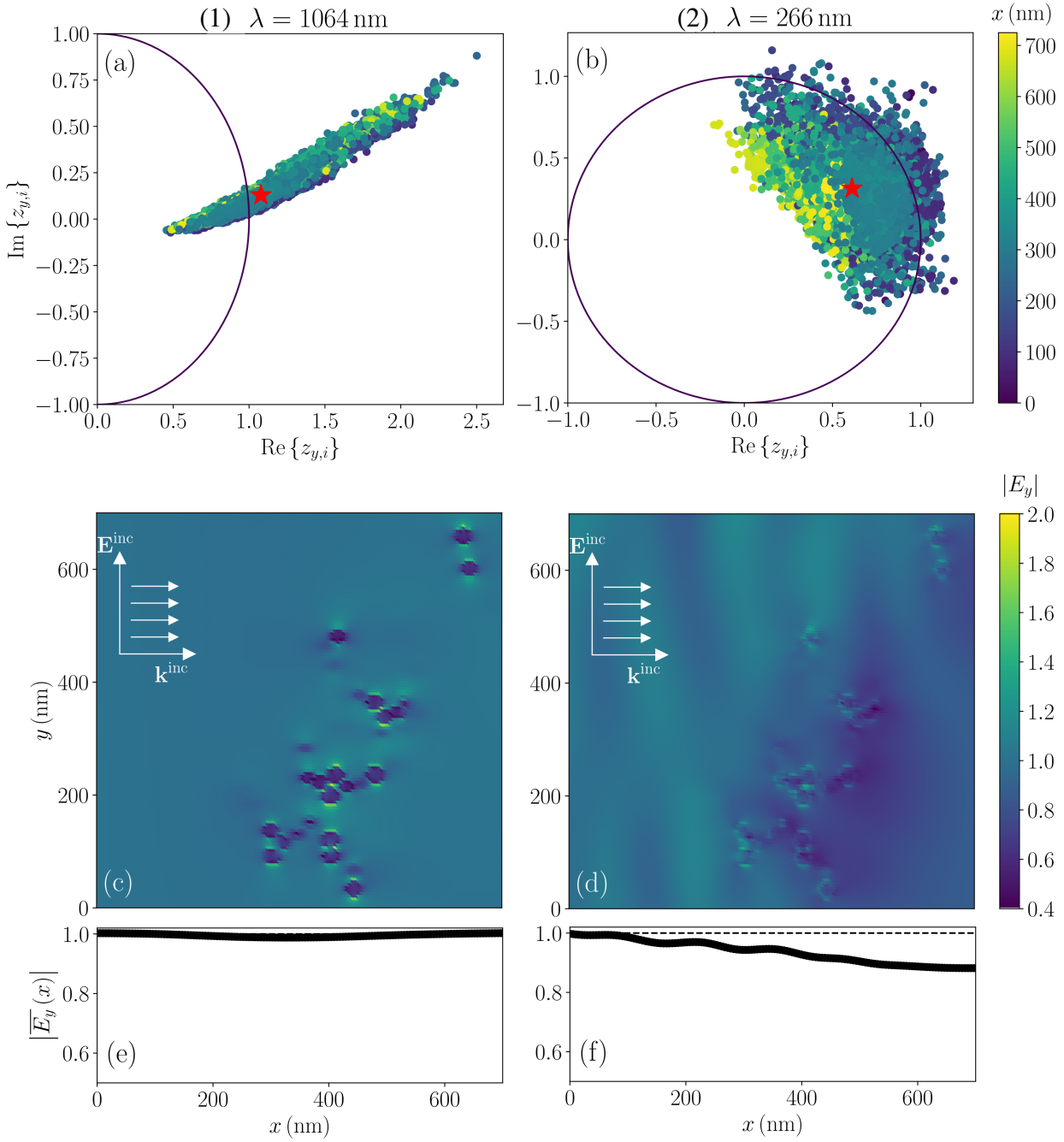

Figure 1: Phasor distributions and internal electric-field analysis of an aggregate composed of $N_{\mathrm{m}} = 284$ monomers with monomer radius $R_{\mathrm{m}} = 15\,\mathrm{nm}$ for organic monomer material. The left column corresponds to $\lambda = 1064\,\mathrm{nm}$ with $m = 1.83{+}i0.26$ whereas the right column corresponds to $\lambda = 266\,\mathrm{nm}$ with $m = 0.94{+}i0.96$. Distributions of the phasors $z_{y,i}$ in the complex plane are shown in (a) and (b) where the semi-circle (or circle) represents unit phasor-magnitude. Each phasor is displayed as a point. The star symbol in each plot represents the average of all the phasors shown, i.e., $\overline{z_y}$. Plots (c) and (d) show the magnitude of the near field and internal field in the x-y plane through the origin. Finally, plots (e) and (f) show the average of the near field taken in the y-z plane for a given x.

scale appearing with the phasor plots. In other words, these colors tag the location of the phasor according to the location's influence (in phase) on the value of $z_{y,i}$. Recall that the x-axis is also the propagation axis for the incident wave (direction of the incident wave vector $\mathbf{k}^{\text{inc}}$). One observes that for $\lambda = 266\,\text{nm}$, Fig. 1(b), there is an overall decrease of the phasor magnitude with increasing x_i. This demonstrates an overall decrease of the internal field magnitude $\left|E_y^{\text{int}}\right|$ along the x-axis, i.e., in the direction that the incident light propagates through the aggregate. For $\lambda = 1064\,\text{nm}$, the same effect is not observed as the full range of phasor-dot colors can be seen throughout the distribution.

Following the resolution of the Maxwell equations inside and outside the scattering object the total electric field everywhere in space is mathematically

$$\mathbf{E}(\mathbf{r}) = \mathbf{E}^{\text{inc}}(\mathbf{r}) + \mathbf{E}^{\text{sca}}(\mathbf{r}), \tag{7}$$

where the scattered electric near-field in discrete form is expressed in terms of the total field inside the scattering object as follows: (see Section 2.1 in [41])

$$\mathbf{E}^{\text{sca}}(\mathbf{r}) = \frac{k^2}{4\pi}\left(m^2 - 1\right)\left(\overleftrightarrow{\mathbf{I}} + \frac{1}{k^2}\nabla \otimes \nabla\right) \cdot \sum_{i=0}^{N} \mathbf{E}^{\text{int}}(\mathbf{r}_i)\frac{e^{ik|\mathbf{r}-\mathbf{r}_i|}}{|\mathbf{r}-\mathbf{r}_i|}\Delta V, \tag{8}$$

with $\otimes$ representing the dyadic product. Note that, the expression of the VIE in Eq. (2) is different from this one due to the far-field zone assumption. Another way to study the overall variation of field magnitude is presented in Figs. 1(c)- 1(d). Here, the magnitude of the y-component of the total electric field, $|E_y| = |\mathbf{E}(\mathbf{r}) \cdot \hat{\mathbf{y}}|$, in the x-y plane through the aggregate is shown. For points not residing in a monomer, the field plotted corresponds to the total near-field, i.e., $|E_y| = \left|E_y^{\text{inc}} + E_y^{\text{sca}}\right|$ whereas $\left|E_y^{\text{int}}\right|$ is plotted for points residing in a monomer. In Fig. 1(c) where $\lambda = 1064\,\text{nm}$, there is little departure from the magnitude of the incident field, $\left|E_y^{\text{inc}}\right| = 1$ except very close to the monomers, i.e., hot spots. However, in Fig. 1(d) where $\lambda = 266\,\text{nm}$, there is structure to this near field extending beyond the monomer length scale.

To better test whether there is an overall trend in near field across the aggregate, Figs. 1(e)-1(f) plot the average of $|E_y|$ within the y-z plane located at x. The result reveals trends of the field magnitude along the x-axis, i.e., along the propagation direction of the incident wave. In Fig. 1(e), the average field is almost invariant from one, which

reveals that the field is close to the magnitude of the incident field across the aggregate. Fig. 1(f), however, shows a clear decay of the field magnitude along x. The decay can be explained by absorption of the incident field; an effect that is neglected by the RDG-FA. Indeed, $\mathrm{Im}\{m\} = 0.96$ for Fig. 1(f), where $\lambda = 266\,\mathrm{nm}$, which is larger than the corresponding value for $\lambda = 1064\,\mathrm{nm}$, i.e., $\mathrm{Im}\{m\} = 0.26$, Fig. 1(e).

To summarize the findings thus far, at large wavelength, the hypothesis of a uniform near-field appears valid. Point contact between the monomers induce local "hot-spots" of the internal electric field (internal coupling), which causes $A > 1$ as revealed by the bi-sphere analysis [21] and the large spread of phasors in Fig. 1(a). At smaller wavelength, the absorption dominates causing $A < 1$ with an effect becoming more marked as the aggregate increases in size. Thus, we qualitatively explain the observations reported in [19, 20].

3.2. Sliced phasors

The qualitative difference between the spread of points in Fig. 1(a) and Fig. 1(b) suggests that the phasors may be helpful to understand the effect of absorption on the RDG-FA correction factors. The effects of absorption are expected to be most noticeable by analyzing the phasors as groups in a way that isolates the absorption-based decay in magnitude of the internal field. Returning to the VIE of Eq. (2), from which the phasors are eventually derived in Eq. (5), one sees that $\mathbf{E}^{\mathrm{int}}$ is accompanied by the term $\exp(-ik\hat{\mathbf{r}}\cdot\mathbf{r}_i)$. When evaluated in the forward-scattering direction, $\hat{\mathbf{r}} = \hat{\mathbf{x}}$, the phase of this term becomes $-ikx_i$, which is a constant across the y-z plane for the given value of x_i; this is why the y-z plane is specifically considered in Fig. 1(e) and Fig. 1(f). The variation in the phasor *magnitudes* corresponding to volume elements in the plane are then only due to the internal field component, E_y^{int}.

With this understanding, let $\Pi(x)$ be the y-z plane at x and define a "sliced phasor" as

$$\overline{z_y(x)} = \frac{1}{N_{\mathrm{d}}(x)} \sum_{\substack{i=1 \\ i\in\Pi(x)}}^{N_{\mathrm{d}}(x)} z_{y,i}(\hat{\mathbf{x}}), \tag{9}$$

where $N_{\mathrm{d}}(x)$ is the number of dipoles (volume elements) of the aggregate that reside in the plane $\Pi(x)$. Equation (9) represents the average of the phasors in the $\Pi(x)$ plane, which means that all of these phasors will have the same phase factor discussed above. Then, sum

all of the sliced phasors for the complete aggregate:

$$z_y(\psi) = \frac{1}{N_\mathrm{d}} \sum_x \overline{z_y(x)} N_\mathrm{d}(x), \tag{10}$$

where ψ expresses the (implicit) aggregate orientation. With this definition, $|z_y(\psi)|^2 = A_\mathrm{vv}(\psi)$ because of the weighting factor $N_\mathrm{d}(x)$ included in Eq. (10), i.e., $\sum_x N_\mathrm{d}(x) = N_\mathrm{d}$.

In order to obtain the RDG-FA correction factor for forward scattering, A, the sliced-phasors must be averaged over aggregate orientation. To do this, the orientation average of a sliced phasor, $\langle \overline{z_y(x)} \rangle_\psi$, is calculated in addition to the orientation average of the number of dipoles $\langle N_\mathrm{d}(x) \rangle_\psi$ in the associated plane $\Pi(x)$. Then, the orientation averaged correction factor is taken as

$$A_\mathrm{vv}^\mathrm{slice} = \left| \frac{1}{N_\mathrm{d}} \sum_x \langle \overline{z_y(x)} \rangle_\psi \, \langle N_\mathrm{d}(x) \rangle_\psi \right|^2, \tag{11}$$

The fact that squaring is done before or after the orientation averaging makes $A_\mathrm{vv}^\mathrm{slice}$ not strictly identical to $\langle A_\mathrm{vv}(\psi) \rangle$ and thus to A. Nevertheless, due to the weak effect of the orientation on the sliced phasors, this approximation is shown to be acceptable as confirmed by Fig. 2 that reports the correlation between the exact forward scattering correction factor A and the newly introduced one based on the orientation averaged sliced phasor $A_\mathrm{vv}^\mathrm{slice}$. The correlation is shown for 4 different DLCA aggregates with different numbers of primary particles ($N_\mathrm{m} = 10$, $N_\mathrm{m} = 100$, $N_\mathrm{m} = 284$, $N_\mathrm{m} = 444$ with a monomer radius $R_\mathrm{m} = 15\,\mathrm{nm}$) by varying the wavelength and the refractive index considering organic, amorphous and graphitic material in respect of the Table 1 in [31]. As can be seen in the figure both quantities are linearly correlated (slope coefficient of 0.994 ± 0.002 with a Pearson's linear coefficient of determination 0.997). This result supports the idea that correction A is only driven by the x dependence of the phasor.

3.3. Effect of monomer number

In this section, the effect of the number of monomers, N_m, on the RDG-FA forward-scattering correction factor is studied in terms of the sliced phasors of Eq. (9). To do this, express a given orientation-averaged slice phasor as:

$$\langle \overline{z_y(x)} \rangle_\psi = \Lambda(x) \exp\left[i\Theta(x) \right], \tag{12}$$

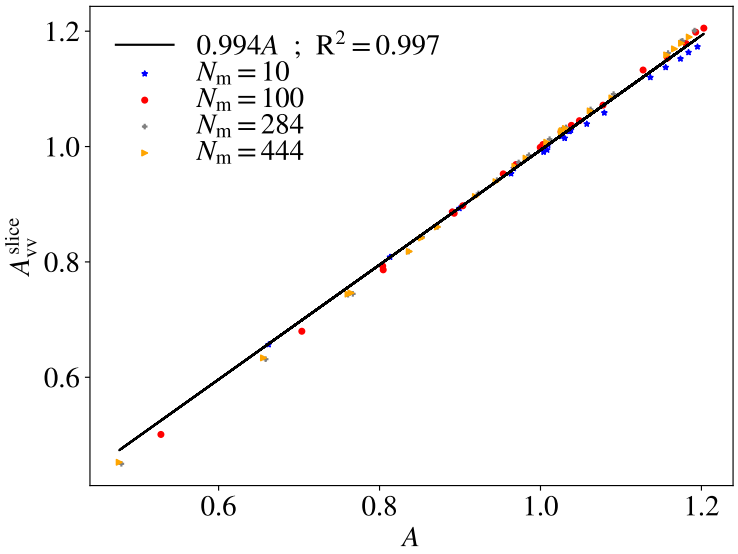

Figure 2: Correlation between the exact forward scattering correction factor A and the newly introduced one based on orientation averaged sliced phasor $A_{\mathrm{vv}}^{\mathrm{slice}}$. A linear regression is displayed in a continuous black line.

where Λ represents the magnitude of the phasor $|\langle\overline{z_y(x)}\rangle_\psi|$ and Θ represents its phase angle $\tan^{-1}\left[\mathrm{Im}\left\{\langle\overline{z_y(x)}\rangle_\psi\right\}/\mathrm{Re}\left\{\langle\overline{z_y(x)}\rangle_\psi\right\}\right]$. Figure 3 shows the Λ in plot (a) and the phase Θ in plot (b) as a function of the coordinate x for the $\Pi(x)$ plane. Here, the x coordinate is normalized by the monomer radius R_{m} rather than the gyration radius R_{g} (see Appendix A), i.e., x/R_{m} where $R_{\mathrm{m}} = 15\,\mathrm{nm}$. Here, six different DLCA aggregates are considered with different N_{m} as indicated. For the illustration, the wavelength and refractive index are, respectively, $\lambda = 266\,\mathrm{nm}$ and $m = 1.75 + 1.03i$. The chosen optical index has been reported recently as a good approximation for mature soot at 550nm [39]. In the following, this optical index will be considered constant at any wavelength when dealing with the parametric study of the wavelength even if the optical index should vary with λ. This dependence to the wavelength will be considered later for graphitic, organic and amorphous materials. In the present case, the shorter wavelength is considered without loss of generality for illustration since RDG-FA is less accurate. As N_{m} increases the larger the aggregate is, and the longer the curve extends along the x/R_{m} axis. One will notice that the curves for Λ show a similar trend overall that appears independent of the aggregate size. The magnitude, Λ in (a), decays with x whereas the phase shift, Θ in (b), grows with x. Recall that the incident wave

propagates along the x-axis, and thus, this decay of Λ is unambiguously due to absorption in the aggregate because of the direct dependence of the sliced phasors on the internal field. The reason that the trends in Fig. 3(a) or Fig. 3(b) are similar is thought to be because the aggregates share similar morphological parameters, D_f, k_f and R_m. In Fig. 3(c) is plotted the average number of dipoles $\langle N_\mathrm{d}(x)\rangle$ in the Π plane at x. The curves grow from zero to a maximum with x and decrease back to zero because Π encompasses more dipoles as it scans from outside the aggregate up to the aggregate's center. The comparison between aggregates and spheres of equivalent volume (equivalent volume radius: $R_\mathrm{v} = N_\mathrm{m}^{1/3} R_\mathrm{m}$) is presented in graphs (a) and (b). The x coordinates of the spheres are normalized by the monomer radius of the aggregates ($R_\mathrm{m} = 15\,\mathrm{nm}$) in order to keep the same scale on the x-axis. Spheres of equivalent volumes show more pronounced trends than aggregates. This is because the volume density of a sphere is higher than that of an aggregate due to the fractal dimension D_f. The denser the material, the more pronounced the absorption and phase shift along the volume.

A general conclusion from Fig. 3 is that whatever the size of the aggregate, the overall behavior of a sliced phasor depends mainly on its distance x into the aggregate. Recalling that the incident wave propagates along x, this behavior is similar to the Beer-Lambert law. Thus, adding more monomers to an aggregate while keeping its D_f, k_f and R_m constant will further decrease the phasor magnitude and increase the phase shift for the largest values of x. In other words, there is a shielding effect that is driven primarily by absorption and not by multiple scattering. This is consistent with findings in [21, 42] where coupling effects are limited several monomer radii for DLCA aggregates. The exception to this behavior is seen when x is small and where Λ exceeds one. Given that $\lambda = 266\,\mathrm{nm}$ and $R_\mathrm{m} = 15\,\mathrm{nm}$, the monomer size-parameter is $x_\mathrm{m} = kR_\mathrm{m} = 0.35$, which from [21] favors the appearance of "hot spots" in the vicinity of point-contact between neighboring monomers.

Nevertheless, at short x, where the quantity of material interacting with the light is reduced and phase shift quite null (b), the amplitude of the phasor can be larger than 1 (notice the amplitude of the incident light E_0 in Eq. (4) is 1). This is explained by the internal coupling enhanced by the contact between spheres. This phenomenon is predominant compared to the self-absorption phenomena only for small x.

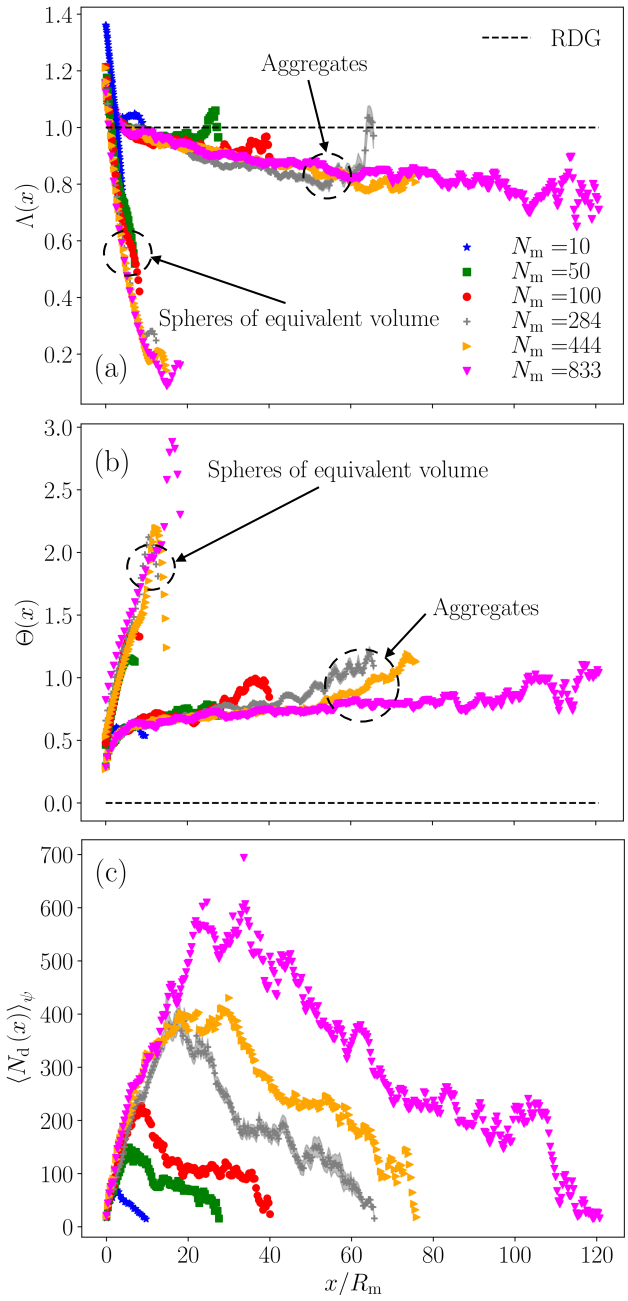

Figure 3: Impact of the number of monomers on the sliced phasor dependence on the position in the aggregates or the spheres of equivalent volume. Plot (a) reports the amplitude $\Lambda(x)$, plot (b) the phase $\Theta(x)$ and plot (c), the averaged number of dipoles per slice. The radius of the monomers of the DLCA aggregates is kept constant ($R_m = 15\,\text{nm}$) as well as the wavelength ($\lambda = 266\,\text{nm}$) and refractive index ($m = 1.75 + i1.03$, [38]). The continuous grey interval surrounding the $N_m = 284$ curve (symbols : plus sign in grey) corresponds to a confidence interval at 95%.

3.4. Effect of monomer size

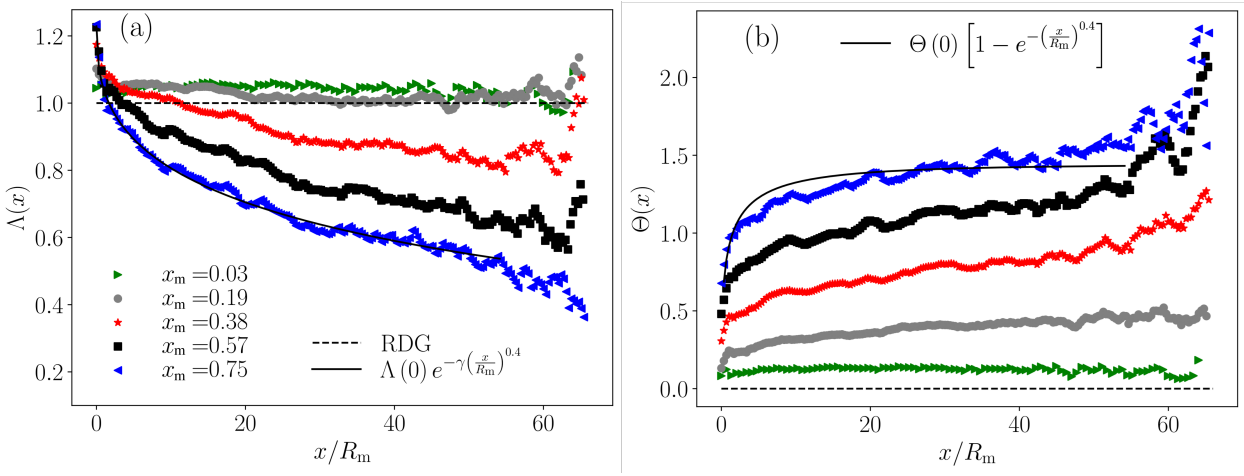

Figure 4: Plots of the amplitude $\Lambda(x)$ (plot (a)) and phase $\Theta(x)$ (plot (b)) versus the normalized axis of the light propagation x/R_{m} of an DLCA aggregate composed of 284 monomers with a monomer radius $R_{\mathrm{m}} = 15\,\mathrm{nm}$ and a refractive index $m = 1.75 + i1.03$ for different size parameters x_{m}. The continuous black lines correspond of an empirical fit of the phasor amplitude by $\Lambda(x) = \Lambda(0)e^{-\gamma\left(\frac{x}{R_{\mathrm{m}}}\right)^{0.4}}$ (a) and its phase by $\Theta(x) = \Theta(0)\left[1 - e^{-\left(\frac{x}{R_{\mathrm{m}}}\right)^{0.4}}\right]$ (b).

To study the effect of monomer size on the sliced phasor behavior, the monomer size parameter $x_{\mathrm{m}} = kR_{\mathrm{m}}$ is varied in Fig. 4 for the same aggregate with $N_{\mathrm{m}} = 284$ for $\lambda = 266\,\mathrm{nm}$ and $m = 1.75 + 1.03i$. This consists of a dilation of the objects which then retain their morphology (N_{m}, D_{f} and k_{f}). Increasing R_{m} will change the internal (dipole-dipole) coupling within the monomers, generally resulting in greater departure of the internal field from the RDG-FA prediction. Increasing R_{m} will also mean absorption will further decrease the phasor magnitudes Λ while increasing their phase Θ. For small $x_{\mathrm{m}} < 0.20$, the impact of absorption is negligible and $\Lambda \sim 1$ (slightly greater than 1 due to the hot spots) and the phase is small, $\Theta << 1$. Thus, $\langle\overline{z_y(x)}\rangle_\psi \approx 1$ and $A \approx 1$, meaning that the RDG-FA is valid. As R_{m} increases, absorption occurs over a larger volume explaining the progressive deviation of $\langle\overline{z_y(x)}\rangle_\psi$ and of A from one, revealing the inaccuracy of the RDG-FA theory. Indeed, [43] shows that the RDG-FA is a reasonable approximation to within 10% error if $x_{\mathrm{m}} < 0.3$.

4. Unification

From Figs. 1-4, one can see the competition between the effects of internal-field enhancements (hot spots), which increase the phasor magnitudes, and absorption, which decreases the phasors magnitudes and increases their phase angle. Absorption explains the aggregate-size dependence of the forward-scattering correction factor for the RDG-FA. Yet both effects are affected by x_{m} and m. As illustrated in Fig. 4, the x dependence of the sliced phasor magnitudes (a) and phasor phase (b) can be fit empirically by

$$\Lambda(x) = \Lambda(0)e^{-\gamma\left(\frac{x}{R_{\mathrm{m}}}\right)^{0.4}} \quad \text{and} \quad \Theta(x) = \Theta(0)\left[1 - e^{-\left(\frac{x}{R_{\mathrm{m}}}\right)^{0.4}}\right]. \tag{13}$$

The functions in Eq. (13) are shown in Fig. 4 by continuous black lines. Note that the fit to $\Lambda(x)$ is an exponential decay, which, again, is reminiscent of the Beer-Lambert for the attenuation of intensity through the aggregate due to absorption.

The phasor-magnitude behaviour is driven by two parameters, namely $\Lambda(0)$ and γ. The former is insensitive to absorption, and thus, only depends on the strength of coupling between monomers and internal coupling within the monomers themselves, i.e., hot spots. The other parameter, γ, is determined by the absorption decay; the greater γ is, the more absorption will be important for the correction factor. With regard to the phase fit in Eq. (13), a single parameter is involved, $\Theta(0)$. This parameter corresponds to the phase shift due to the first plane Π to intersect the aggregate along the x-axis in the direction of propagation of the incident wave. In other words, this part of the aggregate is the first to "see" the wave. Initially the power 0.4 was also considered as a variable parameter but we observed that fixing it at 0.4 had a reduced impact.

Figure 5 reveals a universal behavior of the three governing parameters $\Lambda(0)$, γ and $\Theta(0)$ by varying the wavelength from $\lambda = 266\,\mathrm{nm}$ to $\lambda = 1064\,\mathrm{nm}$. Due to dispersion, m will change with λ and this wavelength dependence is known for graphitic, amorphous, and organic soot material [31]. However, the wavelength dependence also complicates an understanding for how the wavelength affects the fit parameters of Eq. (13). Thus, Fig. 5 considers two cases: The data shown in black triangles shows the fit parameters as λ varies for a *constant* refractive index $m = 1.75 + 1.03i$ in order to isolate the effect of the refractive index. The other data points show the parameters when the wavelength dependence of the

optical index is taken into account.

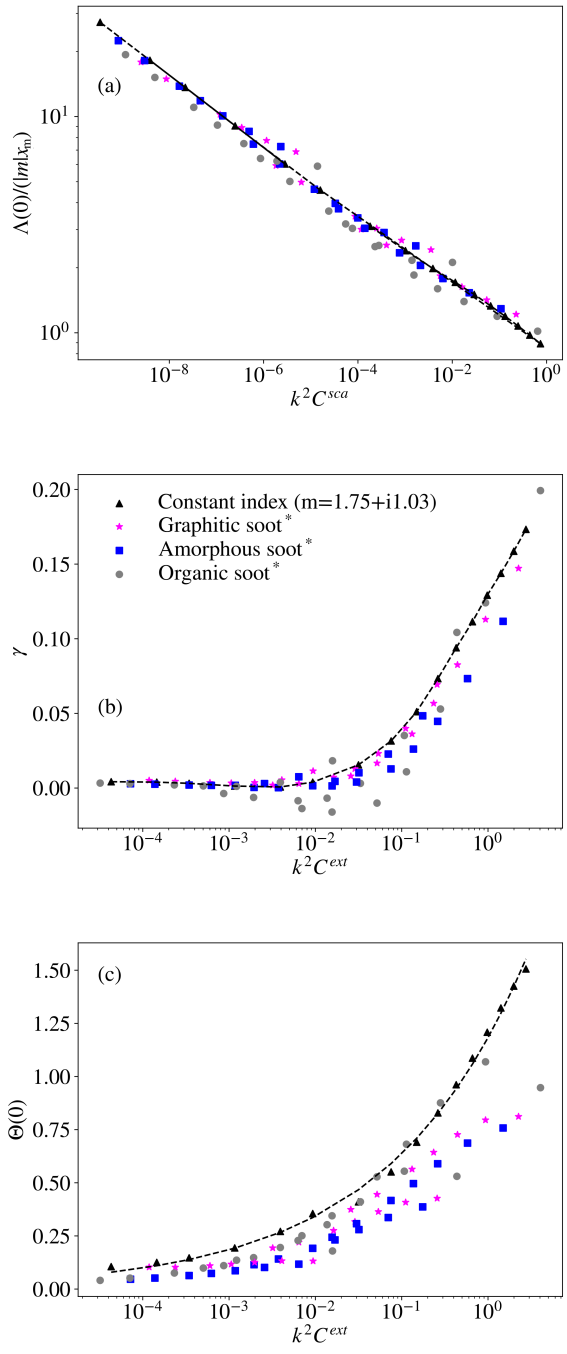

Figure 5: Parameters of the modelled amplitude of the phasor ($\Lambda_i(0)$ and γ) and phase ($\Theta_i(0)$) of the phasor as it evolves by crossing the aggregates. The symbol $*$ in the legend refers to the optical indices provided by Bescond et al.[31] which vary with wavelength.

Recall that $\Lambda(0)$ is driven by the internal coupling between neighboring monomers. Thus,

it seems plausible that this coupling is related to the scattering efficiency of each monomer. This is confirmed by Fig 5(a), where $\Lambda(0)$ is shown normalized by the factor $|m|x_{\mathrm{m}}$ (found empirically) as a function of the dimensionless product k^2C^{sca} where C^{sca} is the total scattering cross section of an isolated monomer in the RDG-FA:

$$C^{\mathrm{sca}} = \frac{8\pi}{3}k^4R_{\mathrm{m}}^6F(m), \qquad C^{\mathrm{abs}} = 4\pi kR_{\mathrm{m}}^3E(m), \qquad C^{\mathrm{ext}} = C^{\mathrm{sca}} + C^{\mathrm{abs}}, \tag{14}$$

where $F(m)$ is the norm squared and $E(m)$ the imaginary part of the Lorentz-Lorenz factor $(m^2-1)/(m^2+2)$. The product of k^2 with the optical cross sections ensures that the scale invariance rule (SIR) [44] is obeyed for the case that m is invariant with λ, i.e., in our case $m = 1.75 + i1.03$. Note that the linear dependence observed in the log-log plot (a) is dominated by the λ dependence for fixed m and R_{m}.

Fig 5(b) shows the behaviour of γ, which represents absorption in the aggregate, and thus, should be function of the extinction cross section C^{ext} of the monomers via Eq. (14). Obviously, the more the monomers absorb, the greater the C^{ext}, and the more efficient light is removed by the entire aggregate. The effect is not linear and absorption appears significant for $k^2C^{\mathrm{ext}} \geq 0.02$. Note that negative values are shown in (b), in particular for the organic material. This means that the amplitude of the phasor tends to increase leading to $A \geq 1$ (as already observed in Fig. 13 of [20]). In that case, local "hot-spots" of the internal electric field dominate the absorption. Figure 5(c) shows that the phase shift induced by the aggregate depends on its capacity to extinguish the light.

Despite the quasi-universal behaviour in Fig 5, the detailed behavior of the data is not perfect due to dispersion, $m(\lambda)$. Dispersion violates the standardization predicted by use of the SIR. Indeed, the reader can observe that the curve corresponding to constant refractive index (black triangles) is perfectly continuous since only the wavelength varies, contrarily to other wavelength-dependent cases.

5. Improved correction of the RDG-FA for forward scattering

Based on the findings above, a semi-empirical model for the correction to the RDG-FA for forward scattering in the vertical-vertical polarization configuration is proposed in Eq. (15). This is a continuous expression of Eq. (11) expressed in terms of amplitude and phase of the

sliced phasor $\langle \overline{z_y}(x) \rangle_\psi$.

$$A_\mathrm{M} = \left| \frac{\int_0^{2R_\mathrm{max}} \Lambda(x) \exp\left[i\Theta(x)\right] \, \mathrm{d}V(x)}{\int_0^{2R_\mathrm{max}} \mathrm{d}V(x)} \right|^2 . \tag{15}$$

Here, R_max is the radius of a sphere encompassing an aggregate, $\mathrm{d}V(x)$ models the volume of material contained in a slice of thickness $\mathrm{d}x$ of the sphere in the y-z plane (see Fig. 6) and the subscript "m" stands for model. Note that, since the volume distribution of the encompassing sphere follows the fractal law its distribution differs from the one of a "full" sphere (see Fig. B.11). The volume element is taken as:

$$\mathrm{d}V(x) = \alpha\left(R_\mathrm{m}, D_\mathrm{f}, \varphi\right) G(x, D_\mathrm{f}, R_\mathrm{m}) \, \mathrm{d}x. \tag{16}$$

where α and G are functions whose development from the fractal scaling law, Eq. (1), are reported in Appendix B. Note that, A_M depends only on G since α in Eq. (16) is independent of x and thus divides out from the fraction in Eq. (15).

Figure 7 shows A_M as a function of the exact correction A for different numbers of monomers per aggregate. For each case, the model is tested by fitting the sliced phasor results as described above for wavelengths between $\lambda = 266\,\mathrm{nm}$ and $\lambda = 1064\,\mathrm{nm}$. As with Fig. 5, dispersion is taken into account here. Even if the model is tested for a large range of wavelengths and covers very different soot material, the agreement is good as the slope is 0.997 ± 0.005.

The model is valid only for $N_\mathrm{m} \geq 10$ corresponding to the minimum aggregate-size that expresses the fractal properties of an aggregate. In order to extend the validity of the model to smaller aggregates, an extended model A_EM is proposed, which empirically forces the correction to one for $N_\mathrm{m} = 1$:

$$A_\mathrm{EM} = A_\mathrm{M}\left(1 - A_\mathrm{M}\right) \exp\left(-\sqrt{\frac{N_\mathrm{m} - 1}{N_\mathrm{c}}}\right), \tag{17}$$

where $N_\mathrm{c} = 9/4$ is related to the critical number of monomers below which the Eq. (15) requires modification.

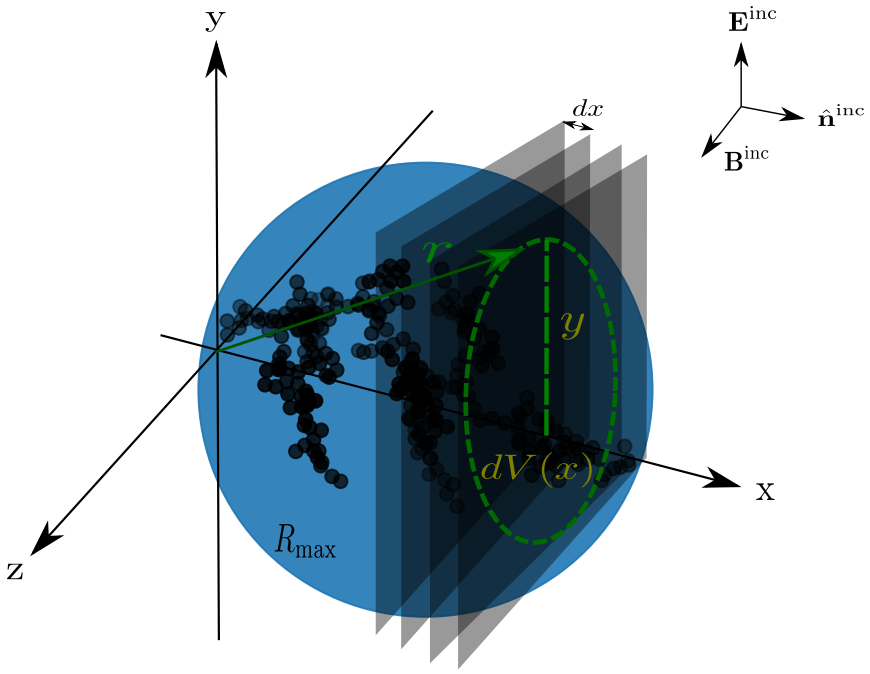

Figure 6: Depiction of the slicing method for the volume of the encompassing sphere of radius R_{max}.

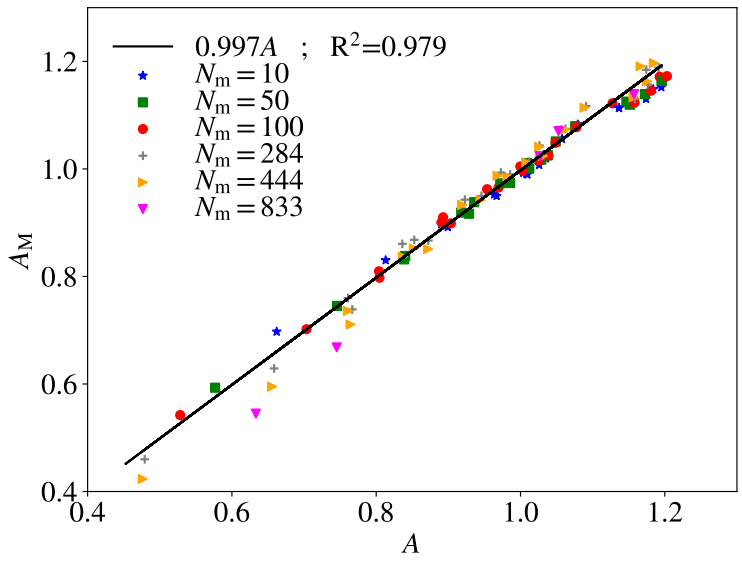

Figure 7: Comparison between the modelled RDG-FA correction for the vertically-vertically polarized forward scattering and the exact one A. The comparison covers the range of wavelengths $266-1064\,\mathrm{nm}$ and the corresponding refractive index for organic, graphitic and amorphous soot material. $R_{\mathrm{m}} = 15\,\mathrm{nm}$. A linear regression is displayed as a continuous black line.

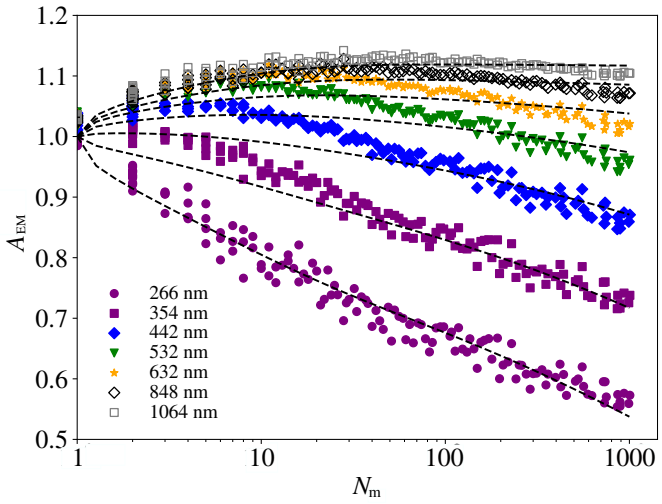

Figure 8: Comparison of the proposed model of correction A_{EM} (dash lines) and the exact correction A (symboles) reported by Yon et al. [19] for Diesel.

Figure 8 shows in symbols the correction factor found by [19] for the same wavelength range as considered here, but with a different m appropriate for Diesel soot. These aggregates are also generated by a DLCA code, i.e., $D_{\mathrm{f}} = 1.78$ and $k_{\mathrm{f}} = 1.44$, but the monomers feature a Gaussian dispersion in size characterized by a mean radius of $\overline{R_{\mathrm{m}}} = 17.1\,\mathrm{nm}$ and a standard deviation of 3.43 nm. To compare to this data, Eq. (15) and Eq. (17) are evaluated by computing the sliced phasor behaviour. An ergodicity hypothesis is made to evaluate the phasors no longer on 500 orientations of the same aggregate but rather on 1000 different aggregates each in a random orientation. These aggregates vary in size, from $N_{\mathrm{m}} = 10$ to $N_{\mathrm{m}} = 1000$, and have a monomer radius $R_{\mathrm{m}} = 17\,\mathrm{nm}$, i.e., the polydispersity of [19] is not taken into account. The results for these 1000 aggregates are reported in dashed lines in Fig 8, where comparison to the [19] data (symbols) illustrates the performance of the proposed model, Eq. (17). The deviations seen can be partially explained by the fact that the polydispersity is neglected and that there is a loss of the fractal nature of the aggregate for small N_{m}. Nevertheless, the new correction factor model, Eq. (17), performs well and is thus useful to extend the range of validity of the RDG-FA to large aggregates for a large range of soot optical properties.

6. Total scattering and absorption

It is reported in [19] that for fractal aggregates multiple scattering mainly affects forward scattering and does not significantly impact the functionality of the phase function, i.e, the structure of the angular scattered intensity. Thus, the total scattering cross section, C^{sca}, can be obtained by applying the same correction factor as above as for forward scattering. Furthermore, a linear relationship between the RDG-FA correction factor for forward scattering and the absorption cross section is empirically observed for soot without coating in [9, 19, 20, 45]. We have recently explained this linearity by showing the absorption cross section correction factor, h, can be formulated in terms of the averaged phasors as

$$h_{\mathrm{v}}(\psi) = \overline{|z_x|^2} + \overline{|z_y|^2} + \overline{|z_z|^2}, \tag{18}$$

where x, y, and z denote the components of the internal electric field used in the phasors, see Appendix F. in [21]. However, as seen in [21], the components $\overline{|z_x|^2}$ and $\overline{|z_z|^2}$ are practically negligible compared to $\overline{|z_y|^2}$ for a bisphere. This seems to be also true for aggregates. Indeed, the contribution of $\overline{|z_x|^2}$ and $\overline{|z_z|^2}$ to the total correction h is evaluated for the aggregate reported in Fig. 1 to be respectively 4% and 3.5% for $\lambda = 266\,\mathrm{nm}$ and 1.6% and 1.6% for $\lambda = 1064\,\mathrm{nm}$. This explains the observed linear relationship between h and A which is proportionnal to $\overline{|z_y|^2}$. Consequently, A_{EM} is linearly connected to h, which can be shown rigorously from the ratio between the DDA absorption cross section and that given by the RDG-FA. This relationship is demonstrated in Fig. 9 for different aggregate sizes for the same range of λ and m as in Fig. 7. The linearity is evident and the slope is similar to that in [19]. Thus, the h correction is simply a multiplication of A_{M} by 1.071 ± 0.007, the slope observed in Fig. 9. For aggregates with small N_{m}, a similar correction to Eq. (17) could be applied.

7. Conclusion

The RDG-FA is a simple theory that is extensively used for the modeling of soot radiative properties and for the interpretation of signals delivered by laser diagnostics. Nevertheless, soot particles and other absorbing aggregates of nanoparticles generally do not fulfill the requirements of the approximation, $x_{\mathrm{m}} \ll 1$ and $|m(\lambda) - 1| \ll 1$, rendering it use in such

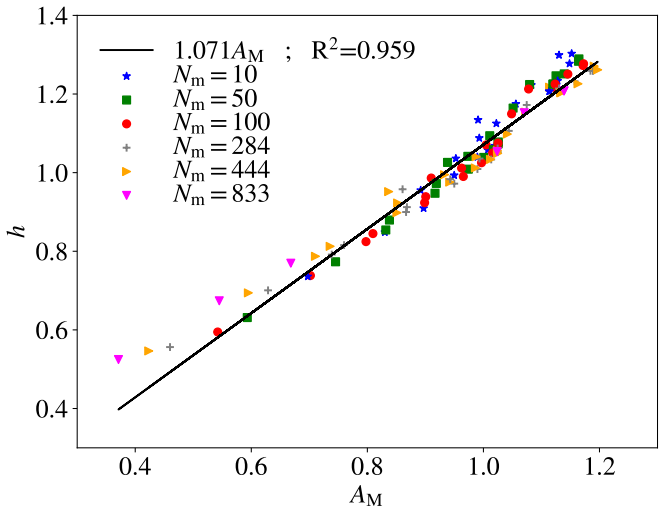

Figure 9: Correlation between the absorption correction factor h and our own model A_M. A linear regression is displayed in a continuous black line.

cases approximate. Indeed, errors up to 60% have been reported. Although deviations between the RDG-FA cross sections and the exact values have been observed in previous works, no model has been proposed to correct them. Our study provides such a correction model valid over a large range of wavelength and for refractive indices relevant to black carbon, organic carbon, graphitic, amorphous, and diesel-like soot materials. The model is made possible by the analysis of the internal electric field using phasors.

Here, to study the behaviour of the internal field as light passes through an aggregate, phasors are averaged in slices through the aggregate, orthogonal to light propagation direction. We see that corrections to the RDG-FA have to take into account two phenomena. First, the internal coupling between monomers is generally a source of field hot-spots in the vicinity of the contact between monomers. Second, absorption decreases the amplitude of the internal field and increases the phase shift as the light propagates through the aggregate. The first phenomenon violates the RDG-FA hypothesis of a uniform internal field and is characterized by a short spatial range. It can explain the underestimation of the RDG-FA cross sections, $A \geq 1$. The second phenomenon violates the hypothesis that each monomer is exposed to the same incident field and explains why the RDG-FA overestimation is enhanced when the number of monomers increases (a shielding effect). Both phenomena and

their dependence on location in the aggregate are analysed through the dependence of three parameters for different wavelengths and refractive indices. Due to the direct relationship between the phasors and the RDG-FA correction factors, this work allows the evaluation of the correction factors for scattering and absorption. The corrections are compared to exact calculations showing good agreement for a wide range of wavelength, aggregate size, and soot material.

Beyond improving our understanding, this work advances the range of validity of the RDG-FA in applications involving soot and BC particles, both in modeling and diagnostics contexts, while also being easy to apply. The reader can download a python script for calculating the corrected RDG-FA based on the current work by using the link https://gitlab.coria-cfd.fr/c-rdgfa/C-RDGFA.

As a pursuit of this work, the current methodology will be applied to more realistic aggregates by considering, for example, monomer polydispersity, necking, overlap and different fractal dimension and prefactor. It could be also adapted to larger range of refractive indices in order to be applicable to other aggregate materials.

Acknowledgments

This work was financed by ANR ASTORIA (N° ANR-18-CE05-0015). The authors thank the CRIANN numerical resources supported by the Normandy, France region. The authors also thank José Moran for providing them with a database of fractal aggregates. MB acknowledges support from the National Science Foundation, awards 1453987 and 1665456, the U.S. Air Force Office of Scientific Research award FA9550-19-1-0078, and the U.S. Army Research Office award FA9550-21-1-0339. RC acknowledges support from ONERA (PROMETE project).

Appendix A. Size normalization

Figure A.10 reports the amplitude of the sliced phasor at the position x by comparing the normalization of this positioning parameter. The left plot normalizes the position x by the gyration radius R_g whereas the right plot considers the monomer radius R_m. As it can be seen the normalization by R_m produced a better unification of the results. The reason of

this better agreement is that R_{m} normalization is representative of the amount of material crossed by the incoming light source whatever the aggregate's size.

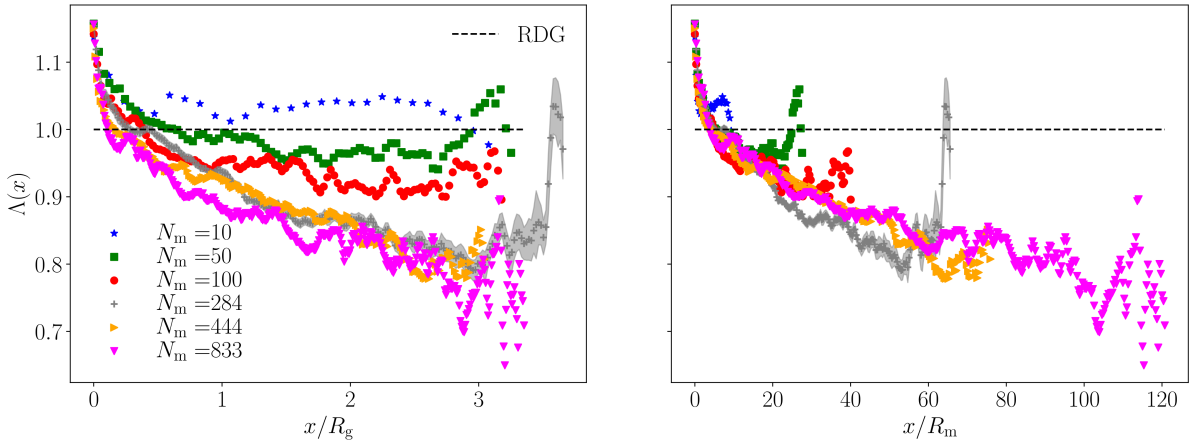

Figure A.10: Impact of the normalization of x by R_{g} or R_{m} on the sliced phasor amplitude $\Lambda(x)$.

Appendix B. Volume distribution

In order to compute A, the phasor approach in slices implies to use the number of dipoles, i.e., the volume in each disk of thickness dx in Fig. 6 as a weighting factor in Eq. (15). We can express the number of monomers of an aggregate of radius R_{max}, contained in a sphere of radius r whose center corresponds to the aggregate center of mass, with $r \in [0, R_{\mathrm{max}}]$ [46]:

$$N_{\mathrm{m}}(r) = \varphi \left(\frac{r}{R_{\mathrm{m}}} \right)^{D_{\mathrm{f}}}. \tag{B.1}$$

In this equation, φ is the packing fraction which represents a local compaction in the aggregate. It is different from the fractal prefactor k_{f} used in Eq. (1) since r is a variable which not corresponds to the gyration radius of the aggregate [34]. From this equation, one can express the probability to find material at a distance r from the aggregate's center of mass:

$$\rho(r) = \frac{1}{4\pi r^2} \frac{\mathrm{d}N_m(r)}{\mathrm{d}r} V_{\mathrm{m}} = \frac{\varphi D_{\mathrm{f}}}{3} \left(\frac{r}{R_{\mathrm{m}}} \right)^{D_{\mathrm{f}}-3}, \tag{B.2}$$

with $(V_{\mathrm{m}} = 4\pi R_{\mathrm{m}}^3/3)$, the volume of a monomer. Therefore, the elementary volume of aggregate in the plane Π corresponding to the green dash circle in Fig. 6, having a radius y

becomes:

$$\mathrm{d}V(x,y) = 2\pi\rho(r)y\mathrm{d}y\mathrm{d}x. \tag{B.3}$$

By integrating this expression in the plane Π, the elementary volume of material contained in a slice of thickness $\mathrm{d}x$ positioned at a distance $x \geq R_\mathrm{m}$ from the left part of the aggregate is:

$$\mathrm{d}V(x) = \underbrace{\frac{2\pi\varphi D_\mathrm{f}\mathrm{d}x}{3R_\mathrm{m}^{D_\mathrm{f}-3}}}_{\alpha(R_\mathrm{m},D_\mathrm{f},\varphi)} \underbrace{\int_0^{\sqrt{r^2-(x-2R_\mathrm{max})^2}} y\left[(x-R_\mathrm{max})^2+y^2\right]^{\frac{D_\mathrm{f}-3}{2}}\mathrm{d}y}_{G(x,D_\mathrm{f},R_\mathrm{m})}. \tag{B.4}$$

By symmetry from the aggregate center of mass, for $x \leq R_\mathrm{m}$, the expression is identical excepted the upper bound of the integral that becomes $\sqrt{r^2-x^2}$.

Fig. B.11 shows the normalized volume distribution $\int_0^{2R_\mathrm{max}} \mathrm{d}V(x)/V$ along the normalized $x/2R_\mathrm{max}$ abscissa for the porous encompassing sphere which models a DLCA aggregate ($D_\mathrm{f} = 1.78$) averaged over orientations and the one from a full sphere (dimension $D_\mathrm{f} = 3$).

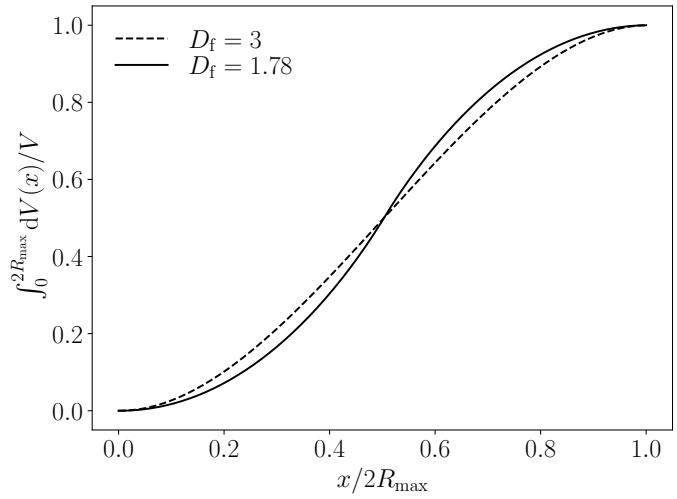

Figure B.11: Normalized volume distribution of the encompassing sphere.

References

[1] A. T. Juarez-Facio, C. Castilla, C. Corbière, H. Lavanant, C. Afonso, C. Morin, N. Merlet-Machour, L. Chevalier, J.-M. Vaugeois, J. Yon, et al., Development of a standardized in vitro approach to evaluate microphysical, chemical, and toxicological

properties of combustion-derived fine and ultrafine particles, Journal of Environmental Sciences 113 (2022) 104–117.

[2] A. Wierzbicka, P. Nilsson, J. Rissler, G. Sallsten, Y. Xu, J. Pagels, M. Albin, K. Österberg, B. Strandberg, A. Eriksson, M. Bohgard, K. Bergemalm-Rynell, A. Gudmundsson, Detailed diesel exhaust characteristics including particle surface area and lung deposited dose for better understanding of health effects in human chamber exposure studies., Atmospheric Environment 86 (2014) 212–219. doi:10.1016/j.atmosenv.2013.11.025.

[3] G. Myhre, F. Stordal, K. Restad, I. S. A. Isaksen, Estimation of the direct radiative forcing due to sulfate and soot aerosols, Tellus B: Chemical and Physical Meteorology 50 (5) (1998) 463–477. arXiv:https://doi.org/10.3402/tellusb.v50i5.16230, doi:10.3402/tellusb.v50i5.16230.
URL https://doi.org/10.3402/tellusb.v50i5.16230

[4] P. J. C. Meinrat O. Andreae, Atmospheric aerosols: Biogeochemical sources and role in atmospheric chemistry 276 (1997). arXiv:https://doi.org/10.1126/science.276.5315.1052, doi:10.1126/science.276.5315.1052.
URL https://doi.org/10.1126/science.276.5315.1052

[5] J. Yon, J. Morán, F. Lespinasse, F. Escudero, G. Godard, M. Mazur, F. Liu, A. Fuentes, Horizontal planar angular light scattering (hpals) characterization of soot produced in a laminar axisymmetric coflow ethylene diffusion flame, Combustion and Flame 232 (2021) 111539.

[6] N. Rattanasom, T. Saowapark, C. Deeprasertkul, Reinforcement of natural rubber with silica/carbon black hybrid filler, Polymer Testing 26 (3) (2007) 369–377. doi:https://doi.org/10.1016/j.polymertesting.2006.12.003.
URL https://www.sciencedirect.com/science/article/pii/S0142941806002182

[7] J. A. Lock, G. Gouesbet, Generalized lorenz–mie theory and applications, Journal of Quantitative Spectroscopy and Radiative Transfer 110 (11) (2009) 800–807, light Scattering: Mie and More Commemorating 100 years of Mie's 1908 publication.

529 doi:https://doi.org/10.1016/j.jqsrt.2008.11.013.
530 URL https://www.sciencedirect.com/science/article/pii/S0022407308002653

531 [8] L. Liu, M. I. Mishchenko, Scattering and radiative properties of complex soot and
532 soot-containing aggregate particles, Journal of Quantitative Spectroscopy and Radiative
533 Transfer 106 (1) (2007) 262 – 273, iX Conference on Electromagnetic and Light Scatter-
534 ing by Non-Spherical Particles. doi:https://doi.org/10.1016/j.jqsrt.2007.01.
535 020.
536 URL http://www.sciencedirect.com/science/article/pii/S0022407307000350

537 [9] J. Yon, A. Bescond, F. Liu, On the radiative properties of soot aggregates part 1:
538 Necking and overlapping, Journal of Quantitative Spectroscopy and Radiative Transfer
539 162 (2015) 197–206.

540 [10] F. Liu, J. Yon, A. Bescond, On the radiative properties of soot aggregates–part 2:
541 Effects of coating, Journal of Quantitative Spectroscopy and Radiative Transfer 172
542 (2016) 134–145.

543 [11] E. M. Purcell, C. R. Pennypacker, Scattering and Absorption of Light by Nonspherical
544 Dielectric Grains, The Astrophysical Journal 186 (1973) 705–714. doi:10.1086/152538.

545 [12] B. T. Draine, The Discrete-Dipole Approximation and Its Application to Interstellar
546 Graphite Grains, The Astrophysical Journal 333 (1988) 848. doi:10.1086/166795.

547 [13] M. A. Yurkin, A. G. Hoekstra, The discrete dipole approximation: An overview and re-
548 cent developments, Journal of Quantitative Spectroscopy and Radiative Transfer 106 (1-
549 3) (2007) 558–589. arXiv:0704.0038, doi:10.1016/j.jqsrt.2007.01.034.

550 [14] M. Lapuerta, S. González-Correa, F. Cereceda-Balic, H. Moosmüller, Comparison of
551 equations used to estimate soot agglomerate absorption efficiency with the rayleigh-
552 debye-gans approximation, Journal of Quantitative Spectroscopy and Radiative Transfer
553 262 (2021) 107522. doi:https://doi.org/10.1016/j.jqsrt.2021.107522.
554 URL https://www.sciencedirect.com/science/article/pii/S0022407321000157

[15] C. F. Bohren, D. R. Huffman, Absorption and scattering of light by small particles, John Wiley & Sons, 2008.

[16] R. J. Hogan, C. D. Westbrook, Equation for the microwave backscatter cross section of aggregate snowflakes using the self-similar rayleigh–gans approximation, Journal of the Atmospheric Sciences 71 (9) (2014) 3292 – 3301. doi:10.1175/JAS-D-13-0347.1.
URL https://journals.ametsoc.org/view/journals/atsc/71/9/jas-d-13-0347.1.xml

[17] C. Sorensen, Light scattering by fractal aggregates: a review, Aerosol Science & Technology 35 (2) (2001) 648–687.

[18] F. Liu, G. J. Smallwood, Effect of aggregation on the absorption cross-section of fractal soot aggregates and its impact on lii modelling, Journal of Quantitative Spectroscopy and Radiative Transfer 111 (2) (2010) 302 – 308, eurotherm Seminar No. 83: Computational Thermal Radiation in Participating Media III. doi:https://doi.org/10.1016/j.jqsrt.2009.06.017.
URL http://www.sciencedirect.com/science/article/pii/S0022407309002325

[19] J. Yon, F. Liu, A. Bescond, C. Caumont-Prim, C. Rozé, F.-X. Ouf, A. Coppalle, Effects of multiple scattering on radiative properties of soot fractal aggregates, Journal of Quantitative Spectroscopy and Radiative Transfer 133 (2014) 374–381.

[20] C. M. Sorensen, J. Yon, F. Liu, J. Maughan, W. R. Heinson, M. J. Berg, Light scattering and absorption by fractal aggregates including soot, Journal of Quantitative Spectroscopy and Radiative Transfer 217 (2018) 459–473.

[21] C. Argentin, M. J. Berg, M. Mazur, R. Ceolato, J. Yon, Assessing the limits of rayleigh–debye–gans theory: Phasor analysis of a bisphere, Journal of Quantitative Spectroscopy and Radiative Transfer 264 (2021) 107550.

[22] R. Ceolato, L. Paulien, J. B. Maughan, C. M. Sorensen, M. J. Berg, Radiative properties of soot fractal superaggregates including backscattering and depolarization, Journal of Quantitative Spectroscopy and Radiative Transfer 247 (2020) 106940. doi:https:

582 //doi.org/10.1016/j.jqsrt.2020.106940.
583 URL http://www.sciencedirect.com/science/article/pii/S0022407319307939

584 [23] M. J. Berg, Power-law patterns in electromagnetic scattering: A selected review and
585 recent progress, Journal of Quantitative Spectroscopy and Radiative Transfer 113 (18)
586 (2012) 2292 – 2309, electromagnetic and Light Scattering by non-spherical particles
587 XIII. doi:https://doi.org/10.1016/j.jqsrt.2012.05.015.
588 URL http://www.sciencedirect.com/science/article/pii/S002240731200266X

589 [24] M. J. Berg, C. M. Sorensen, Internal fields of soot fractal aggregates, Journal of the
590 Optical Society of America. A 30 (10) (2013) 1947–1955. doi:10.1364/JOSAA.30.
591 001947.
592 URL http://josaa.osa.org/abstract.cfm?URI=josaa-30-10-1947

593 [25] M. Berg, C. Sorensen, A. Chakrabarti, Reflection symmetry of a sphere's internal field
594 and its consequences on scattering: A microphysical approach, Journal of the Optical
595 Society of America. A, Optics, image science, and vision 25 (2008) 98–107. doi:10.
596 1364/JOSAA.25.000098.

597 [26] M. J. Berg, C. M. Sorensen, A. Chakrabarti, Explanation of the patterns in mie theory,
598 Journal of Quantitative Spectroscopy and Radiative Transfer 111 (2010) 782–794.

599 [27] P. Meakin, Formation of fractal clusters and networks by irreversible diffusion-limited
600 aggregation, Physical Review Letters 51 (13) (1983) 1119.

601 [28] F. Liu, D. R. Snelling, G. J. Smallwood, Effects of the fractal prefactor on the optical
602 properties of fractal soot aggregates, in: International Conference on Micro/Nanoscale
603 Heat Transfer, Vol. 43901, 2009, pp. 363–371.

604 [29] F. Liu, C. Wong, D. R. Snelling, G. J. Smallwood, Investigation of absorption and
605 scattering properties of soot aggregates of different fractal dimension at 532 nm using
606 rdg and gmm, Aerosol Science and Technology 47 (12) (2013) 1393–1405. arXiv:https:
607 //doi.org/10.1080/02786826.2013.847525, doi:10.1080/02786826.2013.847525.
608 URL https://doi.org/10.1080/02786826.2013.847525

[30] J. Yon, J. J. Cruz, F. Escudero, J. Morán, F. Liu, A. Fuentes, Revealing soot maturity based on multi-wavelength absorption/emission measurements in laminar axisymmetric coflow ethylene diffusion flames, Combustion and Flame 227 (2021) 147–161. doi:https://doi.org/10.1016/j.combustflame.2020.12.049.
URL https://www.sciencedirect.com/science/article/pii/S0010218021000018

[31] A. Bescond, J. Yon, F.-X. Ouf, C. Rozé, A. Coppalle, P. Parent, D. Ferry, C. Laffon, Soot optical properties determined by analyzing extinction spectra in the visible near-uv: Toward an optical speciation according to constituents and structure, Journal of Aerosol Science 101 (2016) 118–132.

[32] H. Chang, T. T. Charalampopoulos, Determination of the Wavelength Dependence of Refractive Indices of Flame Soot, Proceedings of the Royal Society of London Series A 430 (1880) (1990) 577–591. doi:10.1098/rspa.1990.0107.

[33] S. R. Forrest, T. A. Witten Jr, Long-range correlations in smoke-particle aggregates, Journal of Physics A: Mathematical and General 12 (5) (1979) L109.

[34] J. Yon, J. Morán, F.-X. Ouf, M. Mazur, J. Mitchell, From monomers to agglomerates: A generalized model for characterizing the morphology of fractal-like clusters, Journal of Aerosol Science 151 (2021) 105628.

[35] M. I. Mishchenko, Electromagnetic Scattering by Particles and Particle Groups: An Introduction, Cambridge University Press, Cambridge, 2014.

[36] J. D. Jackson, Classical electrodynamics; 2nd ed., Wiley, New York, NY, 1975.
URL https://cds.cern.ch/record/100964

[37] B. T. Draine, P. J. Flatau, Discrete-dipole approximation for scattering calculations, Journal of the Optical Society of America. A 11 (4) (1994) 1491–1499. doi:10.1364/JOSAA.11.001491.
URL http://josaa.osa.org/abstract.cfm?URI=josaa-11-4-1491

[38] T. C. Williams, C. R. Shaddix, K. A. Jensen, J. M. Suo-Anttila, Measurement of the

dimensionless extinction coefficient of soot within laminar diffusion flames, International Journal of Heat and Mass Transfer 50 (7-8) (2007) 1616–1630.

[39] F. Liu, J. Yon, A. Fuentes, P. Lobo, G. J. Smallwood, J. C. Corbin, Review of recent literature on the light absorption properties of black carbon: Refractive index, mass absorption cross section, and absorption function, Aerosol Science and Technology 54 (1) (2020) 33–51.

[40] G. Shu, T. T. Charalampopoulos, Reciprocity theorem for the calculation of average scattering properties of agglomerated particles, Applied Optics 39 (31) (2000) 5827–5833. doi:10.1364/AO.39.005827.
URL http://ao.osa.org/abstract.cfm?URI=ao-39-31-5827

[41] M. I. Mishchenko, L. D. Travis, A. A. Lacis, Scattering, Absorption, and Emission of Light by Small Particles, Cambridge University Press, Cambridge, 2002.

[42] I. Romero, J. Aizpurua, G. W. Bryant, F. J. G. de Abajo, Plasmons in nearly touching metallic nanoparticles: singular response in the limit of touching dimers, Opt. Express 14 (21) (2006) 9988–9999. doi:10.1364/OE.14.009988.
URL http://www.opticsexpress.org/abstract.cfm?URI=oe-14-21-9988

[43] T. L. Farias, Ü. Ö. Köylü, M. d. G. Carvalho, Range of validity of the rayleigh–debye–gans theory for optics of fractal aggregates, Applied optics 35 (33) (1996) 6560–6567.

[44] M. I. Mishchenko, Scale invariance rule in electromagnetic scattering, Journal of Quantitative Spectroscopy and Radiative Transfer 101 (3) (2006) 411 – 415, light in Planetary Atmospheres and Other Particulate Media. doi:https://doi.org/10.1016/j.jqsrt.2006.02.047.
URL http://www.sciencedirect.com/science/article/pii/S0022407306000598

[45] J. Yon, C. Rozé, T. Girasole, A. Coppalle, L. Méès, Extension of rdg-fa for scattering prediction of aggregates of soot taking into account interactions of large monomers, Particle & Particle Systems Characterization 25 (1) (2008) 54–67.

[46] W. Heinson, C. Sorensen, A. Chakrabarti, A three parameter description of the structure of diffusion limited cluster fractal aggregates, Journal of Colloid and Interface Science 375 (1) (2012) 65–69. doi:https://doi.org/10.1016/j.jcis.2012.01.062.
URL https://www.sciencedirect.com/science/article/pii/S0021979712001178